Original Research

Effects of Signal-to-Noise Ratio on the Accuracy and Reproducibility of Diffusion Tensor Imaging–Derived Fractional Anisotropy, Mean Diffusivity, and Principal Eigenvector Measurements at 1.5T

Jonathan A.D. Farrell, BS,[1–3] Bennett A. Landman, MEng,[4] Craig K. Jones, PhD,[1,2] Seth A. Smith, PhD,[1,2] Jerry L. Prince, PhD,[2,4,5] Peter C.M. van Zijl, PhD,[1–3] Susumu Mori, PhD[1,2,4]*

Purpose: To develop an experimental protocol to calculate the precision and accuracy of fractional anisotropy (FA), mean diffusivity (MD), and the orientation of the principal eigenvector (PEV) as a function of the signal-to-noise ratio (SNR) in vivo.

Materials and Methods: A healthy male volunteer was scanned in three separate scanning sessions, yielding a total of 45 diffusion tensor imaging (DTI) scans. To provide FA, MD, and PEV as a function of SNR, sequential scans from a scan session were grouped into nonintersecting sets. Analysis of the accuracy and precision of the DTI-derived contrasts was done in both a voxel-wise and region of interest (ROI)-based manner.

Results: An upward bias of FA and no significant bias in MD were present as SNR decreased, confirming results from simulation-based studies. Notably, while the precision of the PEV became worse at low SNR, no bias in the PEV orientation was observed. Overall, an accurate and precise quantification of FA values in GM requires substantially more SNR than the quantification of white matter (WM) FA values

Conclusion: This study provides guidance for FA, MD, and PEV quantification and a means to investigate the minimal detectable differences within and across scan sessions as a function of SNR.

Key Words: DTI; reproducibility; precision; fractional anisotropy; mean diffusivity; principal eigenvector
J. Magn. Reson. Imaging 2007;26:756–767.

DIFFUSION TENSOR IMAGING (DTI) is an MRI technique that measures the spatial diffusion characteristics of water and provides novel contrasts to study the fiber architecture of the central nervous system in vivo (1–7). The diffusion characteristics of water are dependent on the composition and architecture of the biological environment and can be quantified by scalar and vector contrasts. Prominent scalar quantities include fractional anisotropy (FA), which describes the degree of diffusion anisotropy, and mean diffusivity (MD), which is a measure of the average amount of diffusion in a voxel, both of which have found useful applications in human imaging in the clinic. FA in white matter (WM) arises in part due to axonal and myelin barriers to water diffusion and has been used to assess and monitor WM damage (2,8). MD has been particularly useful in the study of the temporal evolution of stroke (9,10). Recent reviews (2,8,11–14) outline the methodology and clinical applications of DTI.

In addition to scalar quantities, DTI also provides vector contrasts such as the principal eigenvector (PEV) from which the predominant fiber orientation in a voxel can be inferred. The PEV has been used extensively to examine the architecture and connectivity of the brain with color-coded PEV orientation maps (5,15) and tractography methods (11,16–22). DTI continues to grow in

[1]F.M. Kirby Research Center for Functional Brain Imaging, Kennedy Krieger Institute, Baltimore, Maryland, USA.
[2]The Russell H. Morgan Department of Radiology and Radiological Science, The Johns Hopkins University School of Medicine, Baltimore, Maryland, USA.
[3]Department of Biophysics and Biophysical Chemistry, The Johns Hopkins University School of Medicine, Baltimore, Maryland, USA.
[4]Department of Biomedical Engineering, The Johns Hopkins University School of Medicine, Baltimore, Maryland, USA.
[5]Department of Electrical and Computer Engineering, Johns Hopkins University, Baltimore, MD, USA.
Contract grant sponsor: NIH/NCRR; Contract grant number: P41 RR 15241; Contract grant sponsor: NIH: Contract grant numbers: R01 AG20012, U24 RR021382-02.
Preliminary results from this work were presented at Imaging Myelin: Formation, Destruction and Repair, Vancouver, BC, Canada, 2006; as well as at the 14th Annual Scientific Meeting of the International Society for Magnetic Resonance in Medicine, Seattle, Washington, USA, 2006 (Abstract #1075).
*Address reprint requests to: S.M., PhD, The Russell H. Morgan Department of Radiology and Radiological Science, The Johns Hopkins University School of Medicine, 217 Traylor Building, 720 Rutland Avenue, Baltimore, MD 21205. E-mail: susumu@mri.jhu.edu
Received October 31, 2006; Accepted 30 May 2007.
DOI 10.1002/jmri.21053
Published online in Wiley InterScience (www.interscience.wiley.com).

prominence as a research tool and is increasingly included as part of routine clinical MRI protocols.

Quantitative comparison of findings from different DTI experiments is, in principle, feasible. However, it is quite possible that the accuracy and precision of DTI findings could differ substantially, both within and between imaging sites, due to differences in the quantity and quality of the acquired data. This negatively impacts the use of DTI technology in multisite trials, particularly when compatibility is of primary importance, and reduces the confidence in the assessment and monitoring of disease progression in the clinic using DTI contrasts.

Previously, the effects of noise on diffusion anisotropy indices has been investigated in vivo in monkeys (23) and simulation-based studies have investigated the effect of modeled noise (23–27) as well as the choice of b-value (28–30) on a number of DTI-derived contrasts such as eigenvalues, anisotropy indices, and MD. These studies reveal that imaging parameters do indeed have an effect on DTI contrasts and on their relative uncertainty—notably that measured FA values exhibit an upward bias at low signal-to-noise ratio (SNR). The need for a sufficient number of diffusion weighting (DW) directions and the optimal arrangement of the DW scheme has been demonstrated by simulation (29,31,32) and in vivo (32,33). Also, the reproducibility of in vivo DTI measures within subjects and across subjects has been studied (34,35). These previous studies point to the need to develop methods to assess the impact of SNR on individual experiments and to use this information to optimize and coordinate DTI studies across imaging sites.

The objectives of this study were as follows: 1) to establish data acquisition and analysis protocols to investigate the relationship between SNR (scan repetition) and the DTI-derived contrasts of FA, MD, and PEV; 2) to compute the bias (inaccuracy) of these contrasts at low SNR relative to a high SNR gold standard; and 3) to compute the reproducibility (precision) of these contrasts within scanning sessions (intrasession) and between scanning sessions (test-retest). Analysis was done in both a voxel-wise and in a region of interest (ROI)-based manner and results are reported using an extensive and comprehensive set of plots and metrics.

The observed SNR/DTI contrast relationships can be used to identify the minimum SNR requirements necessary to achieve unbiased (accurate) and reproducible measurements and can be used to guide the design of robust DTI protocols, especially for multicenter studies.

MATERIALS AND METHODS

Magnetic Resonance Imaging

A healthy 24-year-old male volunteer participated in this study. Local institutional review board approval and written informed consent were obtained prior to data acquisition. All data were acquired using a 1.5T MR unit (Intera; Philips Medical Systems, Best, The Netherlands) with body coil excitation and an adapted eight-channel phased array sensitivity encoding (SENSE) head-coil (six effective channels) for reception. Three scanning sessions were performed over two days with the subject repositioned between each scan session. A total of 15 DTI datasets were acquired in each of the three scanning sessions, yielding a total of 45 DTI scans.

Each DTI dataset was acquired with the following imaging protocol. A multislice, single-shot echo-planar imaging (EPI) (SENSE factor = 2.0), spin echo sequence (90° flip angle, TR/TE = 3632 msec/100 msec) was used to acquire 25 transverse slices parallel to the line connecting the anterior and posterior commissures, with no slice gap and 2.5 mm nominal isotropic resolution (FOV = 240 × 240, data matrix size = 96 × 96, reconstructed to 256 × 256). DW was applied along 30 directions using the Jones30 scheme (31,32) with a magnetic field gradient strength of G = 19.5 mT/m, yielding a b-factor of 1000 seconds/mm^2 and a diffusion time t_{dif} of approximately 40 ms ($t_{dif} = \Delta - \delta/3$, where Δ is the leading edge spacing, and δ is the duration of the magnetic field gradients, respectively). Five minimally weighted images (five b_0s) ($b \approx 33$ seconds/mm^2) were acquired and averaged on the scanner as part of each DTI dataset. The total scan time to acquire one DTI dataset of 30 diffusion weighted images (DWIs) and 5 b_0s was two minutes 18 seconds. The total time, including image reconstruction, to acquire 15 DTI datasets and an anatomical MRI in a scan session was approximately 45 minutes.

Data Processing

DTI datasets were processed offline using MATLAB (The Mathworks, Natick, MA, USA) routines running on a Sun Fire V880 server (Sun Microsystems Inc., Santa Clara, CA, USA). All data were coregistered with a previously described scheme (36) that utilized FLIRT (FMRIB's Linear Image Registration Tool, The Oxford Centre for Functional Magnetic Resonance Imaging of the Brain [FMRIB], Oxford, UK) (37) to remove rigid body motion. The gradient tables, which specify the direction of the magnetic field gradient corresponding to each particular DWI, were corrected to compensate for the rotational component of the coregistration procedure. These analysis methods were encapsulated as MATLAB code entitled DTI_gradient_table_creator (Johns Hopkins University School of Medicine, Baltimore, MD, USA) and are publicly available (http://www.nbirn.net). Diffusion tensors were calculated using a multivariate log-linear fitting method in which all DWIs and their corresponding vector from the gradient table entered the diffusion tensor calculation as unique entries; i.e., no averaging of DWIs was performed. The log-linear fit was performed with no restriction on the sign of the eigenvalues. To prevent taking the log of zero, all voxels with an intensity of zero in a DWI were set to half of the smallest nonzero voxel intensity recorded. Diagonalization of the diffusion tensor $\bar{\bar{D}}$ produced the three eigenvalues (λ_1, λ_2, λ_3), from which FA and MD were computed (38).

$$FA = \frac{1}{\sqrt{2}} \sqrt{\frac{(\lambda_1 - \lambda_2)^2 + (\lambda_1 - \lambda_3)^2 + (\lambda_2 - \lambda_3)^2}{\lambda_1^2 + \lambda_2^2 + \lambda_3^2}} \quad (1)$$

$$MD = \frac{\text{trace}(\bar{D})}{3} = \frac{\lambda_1 + \lambda_2 + \lambda_3}{3}. \quad (2)$$

The eigenvector associated with the largest eigenvalue (λ_1), i.e., the PEV, is taken to represent the predominant fiber orientation in each voxel. In the color-coded PEV maps, the dominant fiber orientation in a voxel was represented by red, green, and blue colors, which were assigned to right-left, anterior-posterior, and superior-inferior orientations, respectively.

Data Analysis

To provide FA, MD, and PEV as a function of SNR, sequential scans from a scan session were grouped into nonintersecting sets. The grouping method provided N_{obs} = 15, 7, 5, 3, 3, 2, 2, 1, 1, 1, 1, 1, 1, 1, 1 observations of unique sets of 1 through 15 sequential DTI scans (N_{scans}) in each scan session. In all instances the ratio of the number of DWIs to the number of b_0 images (N_{DWI}:N_{b0}) in each set was maintained at 6:1 (31) and subsequent diffusion tensor calculations utilized all DTI data in a given set. The accuracy (i.e., any bias due to low SNR) of the DTI-derived contrasts was assessed relative to the gold standard findings obtained when all 15 DTI acquisitions in a scan session were used in the tensor calculation which are denoted as FA_{gs}, MD_{gs}, and PEV_{gs}, respectively.

The measures computed for FA are discussed below, and an identical analysis was also performed for MD. Given that N FA images were observed for a given level of SNR, the mean value, $\overline{FA}$, standard deviation (SD), $\sigma(FA)$ and coefficient of variation $CV(FA) = 100*\sigma(FA)/\overline{FA}$ were computed for each voxel. Maps of σ(FA) and CV(FA) were computed at SNR levels of 1 through 5 DTI scans, for each scan session.

Precision of FA as a Function of Fiber Orientation

The precision of FA measurements were investigated as a function of the underlying PEV orientation. Analysis was confined to voxels with an $FA_{gs} > 0.25$ in the central 23 of 25 slices for the first scan session. The voxels were sorted into bins according to their PEV_{gs} orientation, using a 5° by 5° spherical coordinate (polar angle ϕ, azimuthal angle θ) grid. As a consequence of this binning procedure, the voxels assigned to a bin share a common fiber orientation. The σ(FA) value computed for each voxel was then sorted accordingly. The average σ(FA) over all the voxels in each bin was then computed. The bin average of σ(FA) is displayed as a function of ϕ and θ as well as on the surface of a sphere (after interpolation). This procedure was performed for SNR levels of one and three DTI scans, respectively.

Intrasession and Test-Retest Reproducibility of FA and MD: Voxelwise Measurements

The precision of FA and MD were computed using a CV metric. The mean CV(FA), and SD of CV(FA), over all voxels within an ROI were computed and are denoted as $\langle CV(FA)\rangle$ and $\sigma(CV(FA))$, respectively. These values were computed, for each scan session independently, at SNR levels of 1 to 5 DTI scans. The values and uncertainty reported in the corresponding section of results are the mean $\langle CV(FA)\rangle$ and the mean $\sigma(CV(FA))$ over all three scan sessions, respectively, at each respective SNR level.

The reproducibility of FA and MD were computed using a test-retest variation metric. Each observation of an FA map in scan session p was paired with a corresponding observation (at the same SNR level) of an FA map in scan session q. The difference between each pairing of FA maps was computed and stored as a vector

$$\text{diff}(FA)_{p,q} = [FA_{1,p} - FA_{1,q}, FA_{2,p} - FA_{2,q}, \ldots, FA_{N,p} - FA_{N,q}]. \quad (3)$$

The test-retest variation of FA measurements in each voxel was computed as the SD of the difference vector at that voxel, divided by the mean value of the FA measured in that voxel across all $2N$ observations in scan sessions p and q:

$$V(FA)_{p,q} = \frac{\sigma(\text{diff}(FA)_{p,q})}{\text{mean}(FA_{p,q})}. \quad (4)$$

A test-retest variation map, $V(FA)_T$, was then calculated across the pairings of scan sessions

$$V(FA)_T = \frac{1}{3}(V(FA)_{1,2} + V(FA)_{2,3} + V(FA)_{1,3}). \quad (5)$$

The values reported in the corresponding results section are the mean $\langle V(FA)_T\rangle$, and SD, $\sigma(V(FA)_T)$, of $V(FA)_T$ over all voxels within an ROI.

Intrasession and Test-Retest Reproducibility of FA and MD: ROI-Based Measurements

The mean FA over all voxels in an ROI is denoted as $\langle FA\rangle$. The mean value, $\langle\overline{FA}\rangle$, the SD, $\sigma(\langle FA\rangle)$ and the $CV_p(\langle FA\rangle)$, of the N observations of $\langle FA\rangle$ at a given SNR level in a scan session p were computed. The values reported in the corresponding results section are the mean $CV_p(\langle FA\rangle)$ over the three scan sessions, $CV_T(\langle FA\rangle)$, and the uncertainty reported is the SD of $CV_p(\langle FA\rangle)$ over the three scan sessions.

Each observation of $\langle FA\rangle$ in scan session p was paired with an observation (at the same SNR level) in scan session q. The difference between each pairing of $\langle FA\rangle$ was computed as

$$\text{diff}(\langle FA\rangle_{p,q}) = [\langle FA\rangle_{1,p} - \langle FA\rangle_{1,q}, \langle FA\rangle_{2,p} - \langle FA\rangle_{2,q}, \ldots, \langle FA\rangle_{N,p} - \langle FA\rangle_{N,q}]. \quad (6)$$

The test-retest variation of ROI-based FA measurements was computed as the SD of the difference vector, divided by the mean value of $\langle FA\rangle$ across all $2N$ observations in scan sessions p and q.

$$V(\langle FA\rangle_{p,q}) = \frac{\sigma(\text{diff}(\langle FA\rangle_{p,q}))}{\text{mean}(\langle FA\rangle_{p,q})}. \quad (7)$$

The test-retest variation values reported in the corresponding results section are

$$V_T = \frac{1}{3}(V(\langle FA\rangle_{1,2}) + V(\langle FA\rangle_{2,3}) + V(\langle FA\rangle_{1,3})) \quad (8)$$

The uncertainty reported is the SD of $V_{p,q}$ over the three scan sessions.

Precision and Accuracy of the PEV Orientation Within a Scan Session

The principal direction of diffusion can be equally well described by the orientation of a PEV with coordinates (x,y,z) and the corresponding antiparallel vector with coordinates (–x,–y,–z). Consequently, the *N* unique observations of the PEV for each voxel must be oriented appropriately to ensure meaningful vector additions and comparisons. To do this, a PEV was selected as a reference vector. Each of the remaining *N*-1 PEVs was set to be the orientation (parallel or anti-parallel) that minimized the angle of separation with respect to the reference vector. The mean of *N* observations of a PEV is computed as the normalized vector sum of components,

$$\overline{\mathrm{PEV}} = \sum_{i=1}^{N} \mathrm{PEV}_i \Big/ \left\| \sum_{i=1}^{N} \mathrm{PEV}_i \right\|, \quad (9)$$

where each PEV has unit length. The angular variation (AV) (i.e., precision) of PEV measurements, in each voxel, was computed as the variation, in degrees,

$$\mathrm{AV} = \frac{1}{\mathrm{N}} \sum_{\mathrm{i}=1}^{\mathrm{N}} \cos^{-1}(\mathrm{PEV}_\mathrm{i} \cdot \overline{\mathrm{PEV}}), \quad (10)$$

of the *N* observations about the observation mean, where · denotes a vector dot product. The AV was calculated at SNR levels of 1 to 5 DTI acquisitions in order to allow at least three independent observations of the PEV orientation in each scan session. The accuracy of a PEV orientation, with respect to PEV_{gs} was computed in each voxel with an angular bias (AB) metric

$$\mathrm{AB} = \cos^{-1}(\overline{\mathrm{PEV}} \cdot \mathrm{PEV}_{gs}) \quad (11)$$

All computations of AV and AB were done on a voxel by voxel basis. The average value, $\langle \mathrm{AB}\rangle_p$ and $\langle \mathrm{AV}\rangle_p$ together with the SD, $\sigma(\mathrm{AB})_p$ and $\sigma(\mathrm{AV})_p$ across all voxels in an ROI were computed for each scan session *p*. This provided metrics for the precision and accuracy of PEV measures, calculated on a voxel-by-voxel basis, averaged over a given anatomical region in each scan session. The AV and uncertainty values reported in the corresponding results section are $\langle \mathrm{AV}\rangle_T$ and $\sigma(\mathrm{AV})_T$, respectively, which are the mean AV and mean $\sigma(\mathrm{AV})_p$ over the three sessions.

Reproducibility of the PEV Orientation Across Scan Sessions

The mean difference, in degrees, between the *i*th observation of a PEV in scan session *p* and the mean PEV in scan session *q* was calculated as:

$$\mathrm{MAD}_{i,p,q} = \cos^{-1}(\mathrm{PEV}_{i,p} \cdot \overline{\mathrm{PEV}_q}). \quad (12)$$

The mean MAD across the pairings of *N* observations was computed as

$$\mathrm{MAD}_{p,q} = \frac{1}{\mathrm{N}} \sum_{i=1}^{\mathrm{N}} \mathrm{MAD}_{i,p,q}, \quad (13)$$

and the mean MAD over the permutations of scan sessions was computed as

$$\mathrm{MAD}_T = \frac{1}{6}(\mathrm{MAD}_{1,2} + \mathrm{MAD}_{2,1} + \mathrm{MAD}_{1,3} + \mathrm{MAD}_{3,1} + \mathrm{MAD}_{2,3} + \mathrm{MAD}_{3,2}) \quad (14)$$

The corresponding section of the results shows the anatomical profile of MAD_T while the values and uncertainty reported are the average value $\langle \mathrm{MAD}_T\rangle$ and SD of $\sigma(\mathrm{MAD}_T)$ over all voxels in an ROI.

Signal to Noise Calculations

The SNR in this study is determined by, and is reported as, the number of DTI datasets (N_{scans}) used in the diffusion tensor calculation (where each dataset consists of 30 DWIs and five b_0s). The computation of a numerical SNR value for DTI experiments is not straightforward because DWIs and b_0 images have different signal intensity and noise profiles. As the SNR in a selected anatomical location in DWIs can depend on the DW direction, the SNR in the b_0 image is typically reported. For comparison, a numerical value for SNR is this study was computed using two sequential observations of the minimally DWIs. First, the average image and the difference image of these two observations were computed. The SNR was then computed as the mean value in an ROI within the average image divided by the standard deviation over the voxels in the same ROI within the difference image. The minimally weighted images from the first 14 scans in the first scan session were paired sequentially, and the SNR in the splenium of the corpus callosum and internal capsule were calculated to be 22 ± 2:1 (approximately 26 dB), and 24 ± 2:1 (approximately 27 dB), respectively. These values reflect the SNR in the scanner average of five b_0 images, which would indicate an approximate SNR of 10:1 (20 dB) in WM structures in a single b_0 image.

RESULTS

SNR Effects on FA Images

Figure 1a shows representative FA maps calculated from one, three, and 15 DTI scans at the level of the lateral ventricles (left) and centrum semiovale (right).

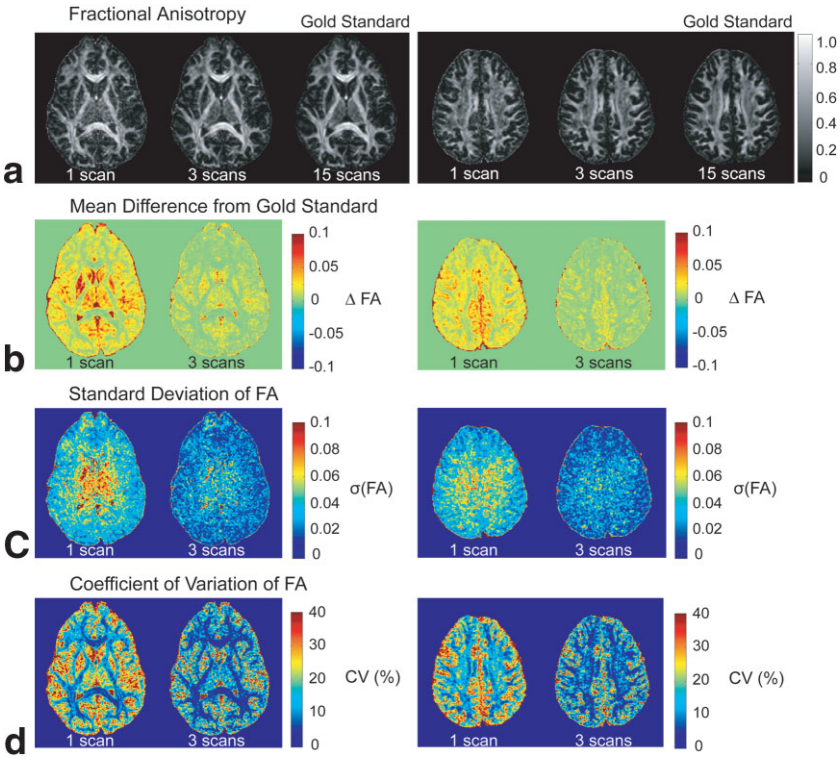

Figure 1. Images showing the relationship between the accuracy and precision of FA and the number of DTI scans used in the diffusion tensor calculation. Results are shown at two slice levels. **a:** Representative FA maps computed from one, three, and 15 DTI scans, respectively. **b:** Difference between the average of 15 FA maps calculated from single DTI scans and the gold standard (left). Difference between the average of 5 FA maps calculated from sets of three DTI scans and the gold standard (right). **c:** SD and (**d**) CV of FA calculated from the 15 observations of FA maps from single DTI scans (left) and the five observations of FA maps calculated from sets of three DTI scans (right).

FA maps calculated from a single DTI scan demonstrate a grainier appearance, indicating increased noise, particularly in gray matter (GM) regions, relative to the gold standard FA map (15 scans). The putamen and globus pallidus have a pronounced speckled appearance in the FA map calculated from one DTI acquisition, whereas the structures are more visually distinct in the FA map from three scans and even more so in the gold standard. Both the visual contrast between GM and WM, and the conspicuity of the boundary between these tissue types in FA maps, improves with increased SNR.

In practice, the quantity of DTI data acquired in a scan session is restricted by the available scan time. If one can acquire multiple repetitions of a DTI acquisition, a pertinent question is whether it is better to average the processed FA maps, or to use all acquired data, after motion correction, in one diffusion tensor calculation. In the context of 15 acquired DTI scans, the former approach implies calculating the average of N_{obs} FA maps, where each FA map is computed from N_{scans} respectively (results are shown for $N_{obs} = 15$, $N_{scans} = 1$ and $N_{obs} = 5$, $N_{scans} = 3$), while the latter approach implies using all 15 datasets (gold standard) in a single tensor calculation. Figure 1b shows the difference between these two DTI processing methods at two SNR levels. The results indicate that taking the average of FA maps reinforces the upward FA bias (which is already present in the individual FA maps themselves) in GM regions. The upward FA bias, relative to the gold standard FA map, is diminished when more data is used in the tensor calculation.

Figure 1c and d show the SD, σ(FA), and the CV(FA) of multiple observations of FA maps computed from single DTI scans ($N_{obs} = 15$, $N_{scans} = 1$, left) and three DTI scans ($N_{obs} = 5$, $N_{scans} = 3$, right). σ(FA), increases—i.e., precision worsens—with penetration depth from the receive coil elements. Using three scans, σ(FA) decreases globally. Figure 1d shows that the CV(FA) is larger in deep GM (putamen) than in adjacent WM (internal capsule), despite the fact that both tissue types are approximately equidistant from the receive coil elements. This occurs because the SD of FA measurements in GM is a larger fraction of the underlying FA value than the SD of FA measurements in WM. Regions of the brain that benefit most from the increased SNR include regions far from the receive coil elements (e.g., deep structures). The effects of SNR on MD were much smaller (for the range of SNR investigated) and were not easily visually appreciated in the MD images (images not shown).

Precision of FA as a Function of Fiber Orientation

To determine if the 30 orientation DW scheme used for this study provided a uniform precision profile in vivo, the standard deviation of FA measurements was computed and displayed as a function of the underlying PEV orientation. Figure 2a shows a relatively constant value of σ(FA) indicating that the precision of voxel-wise FA measurements are not substantially dependent on the underlying fiber orientation at an SNR level of 1 DTI scan. When three DTI scans are used to calculate the diffusion tensor, the precision of FA measurements improves (i.e., σ(FA) decreases) for all fiber orientations. These results agree with previous simulation results (i.e., Jones (29) and Skare et al (32)), which points out the benefit of using a DW scheme with high directional resolution. Figure 2b shows the data from Fig. 2a represented on the surface of a sphere, with the location of the DW directions given by solid markers.

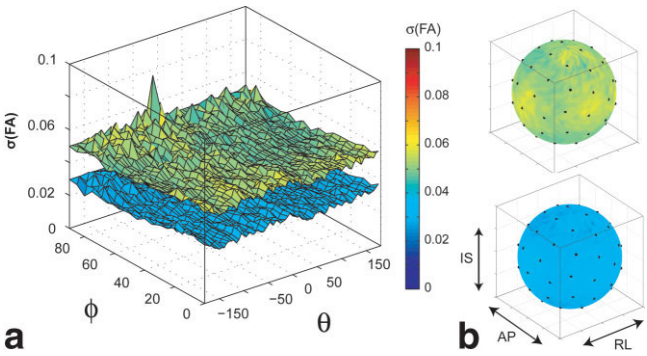

Figure 2. The SD of voxel-wise FA measures in WM ($FA_{gs} > 0.25$) displayed as a function of fiber orientation. **a:** σ(FA) computed from single DTI scans and from sets of three DTI scans, top and bottom surfaces, respectively. **b:** Results from (a) represented on the surface of a sphere with the DW directions (solid markers). The patient coordinate system is abbreviated as inferior-superior (IS), anterior-posterior (AP), and right-left (RL).

Accuracy of ROI-Based FA and MD Measurements

The effects of SNR on ROI-based measures of FA and MD were investigated with manually-defined ROIs in the putamen, globus pallidus, centrum semiovale, internal capsule, and splenium of the corpus callosum. These ROIs are shown in Fig. 3 and included 143, 180, 158, 151, and 237 voxels, respectively. The mean FA in each ROI is shown in Fig. 4a and demonstrates a reproducible upward bias of FA at low SNR, with respect to the gold standard, in deep GM structures (putamen and globus pallidus), which is consistent in all three scan sessions. Notably, dense WM regions such as the internal capsule, and splenium of the corpus callosum together with less anisotropic WM structures like the centrum semiovale exhibited no FA bias at low SNR. Analysis of FA and MD in the frontal WM ROI is not reported as this is a region of crossing fibers; however this region is used for subsequent voxel-wise PEV analysis.

A more comprehensive analysis of the ROI-based FA results is given in Fig. 4b. All data points from the three scan sessions in Fig. 4a are consolidated to a representative single value in Fig. 4b (solid circles). The spread of the FA values in Fig. 4a was computed as the SD of all points over all sessions and is shown as dotted lines in Fig. 4b. Lastly, the SD of FA measurements within each ROI was computed and averaged over all observations in all sessions (shown as error bars in Fig. 4b). Figure 4b shows that the uncertainty associated with determining the ROI-based FA value is small, as indicated by the small range of the dotted lines. Also, the SD of FA values within the ROI is large, even at high SNR.

In contrast to the results observed for FA, no bias trend at low SNR was observed for MD. Due to the small dynamic range of MD across different brain regions, the data series for ROIs in the putamen and centrum semiovale are shown as representative GM and WM structures, respectively. Figure 4c shows that although the variability associated with the determination of the mean value of MD in an ROI increases (widening of the envelope of data points), no bias trend of MD was observed at low SNR. The data in Fig. 4c is consolidated in Fig. 4d in a similar fashion, as was discussed for the ROI-based FA analysis.

The diffusivity of each eigenvalue was averaged separately over all voxels within an ROI in the putamen, a relatively isotropic diffusion medium. Figure 5a and b show a reproducible upward bias of the diffusivity for λ_1, while λ_2 remains fairly stable and λ_3 exhibits a downward bias. This eigenvalue repulsion trend, in the context of the equations for FA and MD, accounts for the observed increase in FA and corresponding stable MD as a function of SNR in low FA structures. In the case of the internal capsule, a more anisotropic medium, the diffusivity of the eigenvalues remained stable, and hence the FA and MD in WM structures exhibited no bias trends throughout the range of SNR investigated in this study (Fig. 5c and d).

Reproducibility of Voxel-Wise FA and MD Measurements

The reproducibility of voxel-wise measures of FA and MD within a scan session was investigated using a CV metric. Figure 6a shows a large disparity, between GM and WM, of the intrasession reproducibility of voxel-wise measures of FA. Though both improve as a function of SNR, voxel-wise measures of FA were less reproducible in GM than in WM. Figure 6b shows that voxel-wise measures of MD are comparable in GM and WM and are more reproducibility than those of FA.

The reproducibility of voxel-wise measures of FA and MD across scan sessions was investigated using a test-retest variation (V) metric. Mirroring the trend observed for the intra-session results, Fig. 6c shows a large disparity between the test-retest reproducibility of voxel-wise measures of FA in GM and WM. Figure 6d shows that the test-retest reproducibility of voxel measures of MD is comparable in GM and WM.

Reproducibility of ROI-Based FA and MD Measurements

The effect of SNR on the reproducibility of ROI-based measurements of FA and MD within a scan session was investigated using a CV metric. Figure 7a shows a disparity, between GM and WM, in the reproducibility of ROI-based measures of FA within scan sessions. Figure 7b shows that the reproducibility of ROI-based mea-

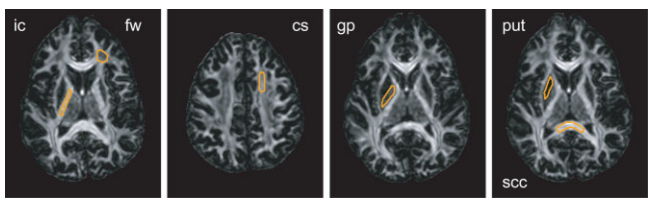

Figure 3. Locations of ROIs at four slice levels used for ROI-based analyses. These include internal capsule (ic), frontal white matter (fw), centrum semiovale (cs), globus pallidus (gp), putamen (put), and splenium of the corpus callosum (scc).

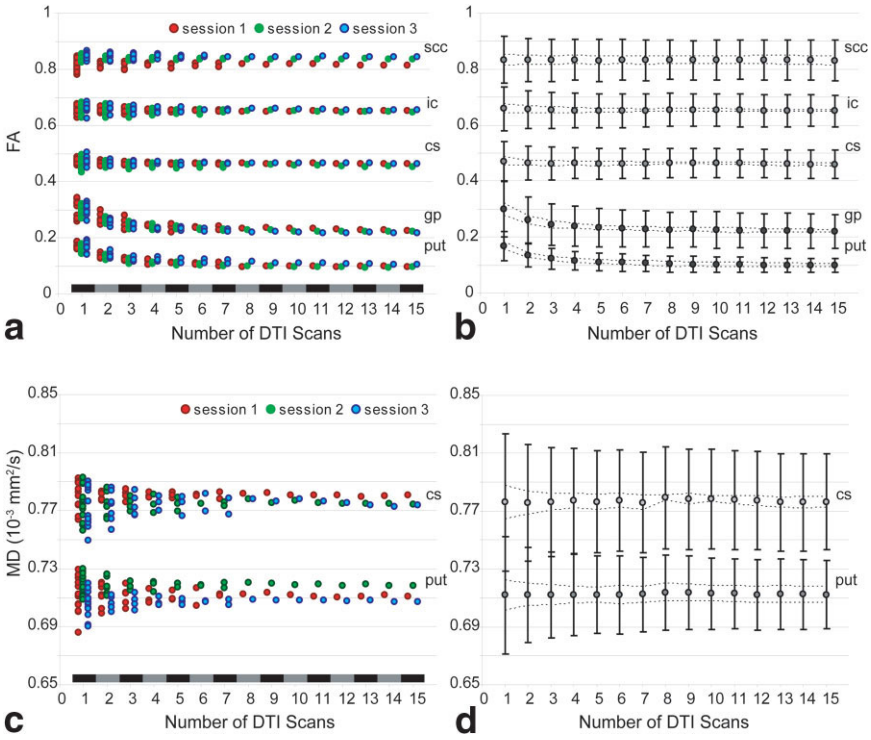

Figure 4. ROI-based FA and MD as a function of the number of scans. **a:** The mean FA in an ROI and (**c**) the mean MD in an ROI for each unique grouping of DTI data (solid circles). The three scan sessions are represented by red, green, and blue solid circles. **b**,**d:** All data points from the three scan sessions in (a) and (c) are consolidated to representative single values in (b) and (d), respectively (solid circles). The spread of the FA measurements in (a) and the spread of MD measurements in (c) were computed as the SD of all points over all sessions (shown as dotted lines). The SD of FA measurements within each ROI in (a) was computed and averaged over all observations in all sessions (shown as error bars). **d:** The corresponding results for MD. Anatomical locations and abbreviations are shown in Fig. 3. [Color figure can be viewed in the online issue, which is available at www.interscience.wiley.com.]

sures of MD within scan sessions was comparable for all regions investigated.

The reproducibility of ROI-based measures of FA and MD across scan sessions was investigated using a test-retest variation (V) metric. Figure 7c shows that ROI-based measures of FA were less reproducible across scan sessions in GM than in WM. Figure 7d shows that, as in the intrasession results, the test-retest reproducibility of ROI-based measures of MD in GM and WM are comparable for all regions investigated.

Reproducibility and Accuracy of the PEV Orientation

Representative color coded PEV orientation maps calculated from one, three, and 15 DTI scans from a single scan session are shown in Fig. 8a. The images show that increased SNR improves the visual definition of WM fiber bundles. Structures such as the anterior and posterior limbs of the internal capsule, together with the centrum semiovale, have a speckled appearance in

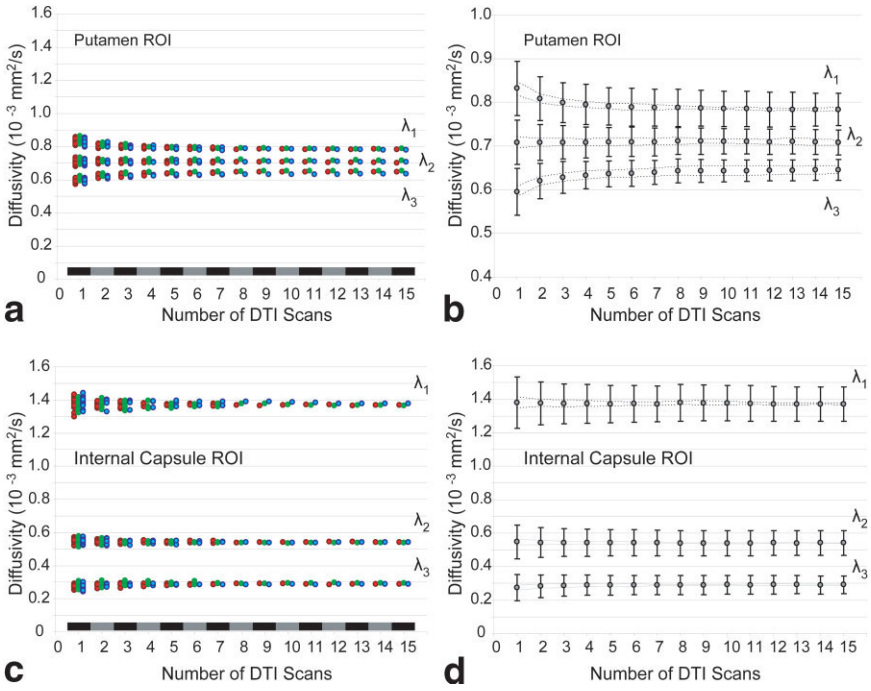

Figure 5. ROI-based eigenvalues (λ_1, λ_2, and λ_3) as a function of the number of scans. **a:** The mean eigenvalue in the putamen and (**c**) the mean eigenvalue in the internal capsule, for each unique grouping of DTI data. The three scan sessions are represented by red, green, and blue solid circles. **b**,**d:** All data points from the three scan sessions in (a) and (c) are consolidated to representative single values in (b) and (d), respectively (solid circles). The spread of the eigenvalue measurements in (a) and (c) were computed as the SD of all points over all sessions (shown as dotted lines). The SD of the eigenvalue measurements in the putamen ROI in (a) was computed and averaged over all observations in all sessions (shown as error bars). d: Shows the corresponding results for the internal capsule ROI. Anatomical locations and abbreviations are shown in Fig. 3. [Color figure can be viewed in the online issue, which is available at www.interscience.wiley.com.]

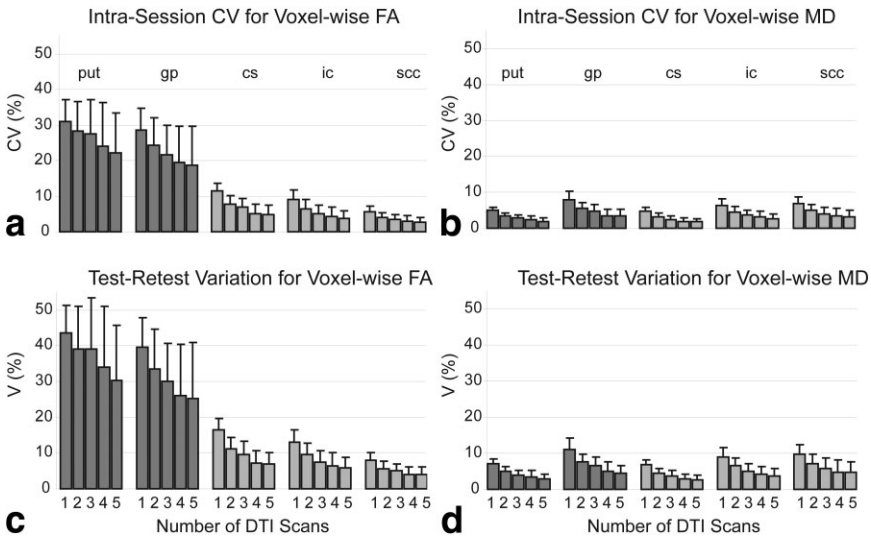

Figure 6. Reproducibility of voxel-wise FA and MD measurements. Intrasession reproducibility: (**a**) CV of FA; (**b**) CV of MD. Intersession reproducibility: (**c**) test-retest variation of FA; (**d**) test-retest variation of MD. Anatomical locations and abbreviations are shown in Fig. 3.

the image computed from a single DTI scan whereas these structures appear more homogenous at higher SNR. Additionally, the U-fiber projections into cortical GM regions are more clearly defined on the higher SNR PEV colormaps. Though the benefits of increased SNR can be visually appreciated, the reproducibility and potential bias of the PEV as a function of SNR are difficult to discern in the PEV color maps themselves. A quantitative assessment of PEV precision, accuracy and across session reproducibility was performed on a voxel by voxel basis in several WM fiber bundles.

An AV metric was used to compute the precision of PEV orientations within a scan session. The AV can be interpreted as the spread, in degrees, of individual observations from the observation mean. Figure 8b shows that the precision of the PEV orientation improved as a function of SNR, with an approximate two-fold improvement in precision when three DTI scans were used to calculate the diffusion tensor, relative to PEV maps that used one DTI scan.

The accuracy of the PEV was computed using an AB metric. The AB is defined as the difference, in degrees, between the mean observation of a PEV at a given SNR level and the gold standard PEV in the same voxel. The accuracy of the PEV orientation is robust across the range of SNR investigated, with no discernable bias at low SNR for the WM structures investigated (Fig. 8c).

Lastly, the test-retest reproducibility of the PEV orientation across scan sessions was investigated using a mean angular difference (MAD) metric. This metric can be interpreted as the combined error of the PEV orientation across scan sessions, with contributions from poor accuracy and poor precision. Increased SNR improves the reproducibility of the PEV orientation in WM (Fig. 9a) with marked improvement in the test-retest reproducibility of the PEV orientation, particularly in the frontal and posterior WM regions. For the major WM tracts investigated, the improvement in across-session reproducibility of the PEV's was less pronounced (Fig. 9b).

DISCUSSION

In this work, which is part of a series of in vivo human DTI calibration studies through The Biomedical Infor-

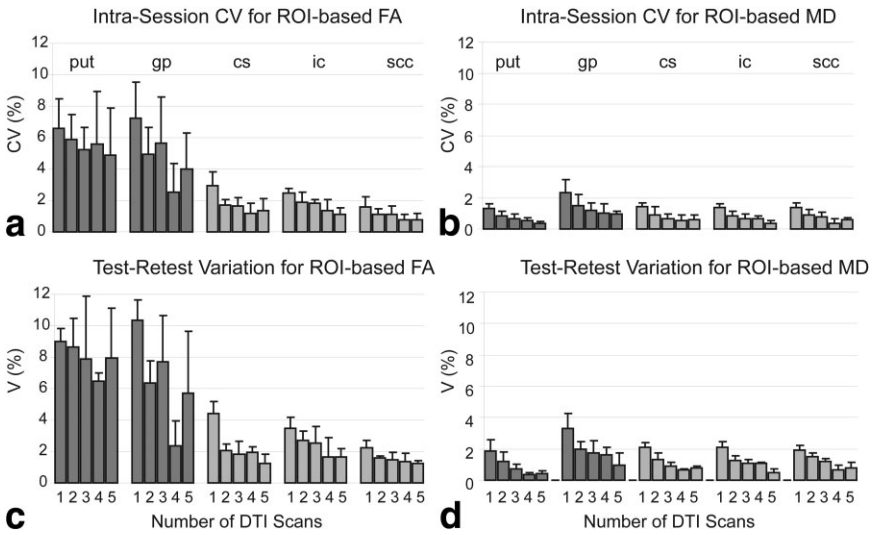

Figure 7. Reproducibility of ROI-based FA and MD measurements. Intrasession reproducibility: (**a**) CV of FA; (**b**) CV of MD. Intersession reproducibility: (**c**) test-retest variation of FA; (**d**) test-retest variation of MD. Anatomical locations and abbreviations are shown in Fig. 3.

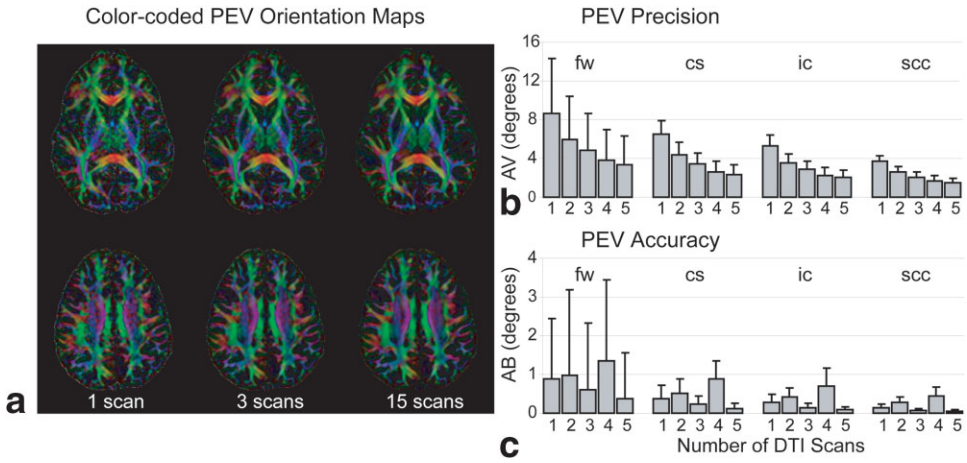

Figure 8. Improvements in color-coded PEV orientation maps as a function of the number of scans. **a:** Representative PEV orientation maps computed from one, three and 15 DTI scans, at two-slice levels. The precision and accuracy of the PEV orientation within a scan session were computed on a voxel by voxel basis in four anatomical regions. **b:** Angular variation (AV) and (**c**) angular bias (AB) of the PEV as a function of SNR. Anatomical locations and abbreviations are shown in Fig. 3.

matics Research Network (BIRN; http://www.nbirn.net), data acquisition and analysis protocols were established to investigate the relationship between DTI scan repetition (i.e., SNR) and the contrasts of FA, MD, and PEV. With several unique observations of the DTI contrasts at each SNR level, we compute the bias (inaccuracy) in these contrasts at low SNR relative to a high SNR gold standard and compute the reproducibility (precision) of FA, MD, and PEV measures within a scan session (intrasession) and between scan sessions (test-retest). The DTI acquisition protocol used in this study was adopted for three reasons. First, simulation-based studies suggest that a DW scheme with about 30 unique directions is required to ensure a uniform precision profile of FA measurements (29,31,32). Second, the optimal ratio of the number of DWIs to minimally weighted images has been shown to be approximately 9:1 (31). Third, we believed that this scan protocol, with a moderate TE (100 msec), moderate gradient strength (19.5 mT/m), and 2.5 mm isotropic resolution should be well accepted as a clinically achievable DTI study at 1.5T. The imaging protocol for this study can be extended to whole brain coverage with an approximate total scan time of five minutes per DTI acquisition.

It is well known that cardiac pulsation often has a profound effect on DTI results (39–41), which could be a major contribution to intra- and intersession reproducibility. Unfortunately, cardiac gating has not been widely accepted in clinical studies because of lengthening of the scanning time and occasional instability of gating depending on subject conditions such as arrhythmia. In this study, we decided not to use cardiac gating to represent more common imaging protocols.

A concurrent goal of this work is that the acquired and processed DTI data, observed relationships between SNR and DTI contrasts, and the acquisition protocol for this study be made available as data resource and reference to establish robust DTI protocols, especially for multisite studies. To facilitate the use of our in vivo human DTI calibration study for this purpose, the information is freely available through the BIRN website (http://www.nbirn.net) and can be used as a data resource and reference for a 1.5T scanner.

The comparison of SNR values from simulation based studies with those of experimentally acquired MR data, or between different sets of MR data from different sites, is not straightforward and should be made with care. Whereas the noise in simulation based studies is a modeled parameter, data from MR scanners can be susceptible to artifacts due to nonuniform receive coil sensitivity, chemical shift artifacts, field inhomogeneity, eddy current distortions, EPI-based susceptibility

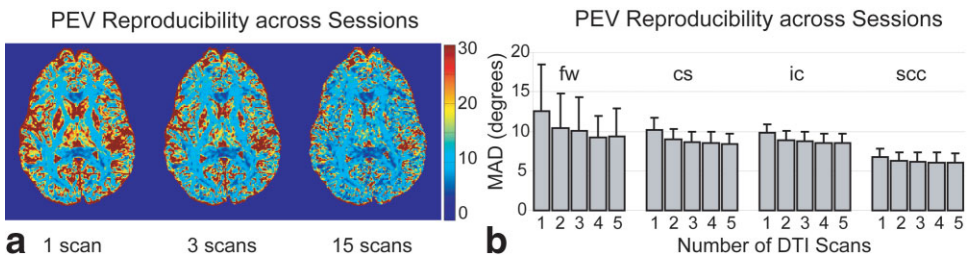

Figure 9. Reproducibility of the PEV orientation across scan sessions. **a:** The spatial distribution of the mean angular difference (MAD) of PEV maps computed using sets of one, three, and 15 scans. **b:** MAD as a function of the number of scans for four anatomical regions. Anatomical locations and abbreviations are shown in Fig. 3. [Color figure can be viewed in the online issue, which is available at www.interscience.wiley.com.]

artifacts, and subject motion. Additionally, parallel imaging techniques with phased-array coils produce an inhomogeneous SNR profile, with regions closer to the reception elements having a higher SNR. In DTI experiments, it is not clear how to compute SNR because diffusion-weighted and non-diffusion-weighted (b_0) images have different signal intensity and noise profiles. As the SNR in a selected anatomical location in DWIs can depend on the DW direction, the SNR in the b_0 image is typically reported. For comparison, the SNR in a single b_0 image was reported for ROIs in the splenium of the corpus callosum and internal capsule. It is expected that SNR will scale, at best, with the square root of the number of DTI acquisitions used in the diffusion tensor calculation. However, differences in hardware performance means that it is unlikely that the same number of DTI acquisitions with a common protocol at two imaging sites will yield compatible results. Therefore, an important recommendation of this study is that each site that participates in a collective study should investigate the SNR/DTI contrast relationship on their MR system as a function of scan repetition, with a common protocol. This will enable each imaging site to calibrate their acquisition to meet the SNR requirements given by the study coordinators. This could be combined with the use of a traveling human volunteer, or a standardized nonhuman phantom.

Low SNR typically has detrimental effects on the precision of a given measurement, while the accuracy is generally unaffected. However, DTI-based contrasts can suffer from poor accuracy in addition to the expected loss of precision at low SNR. We confirmed that low SNR increases the noise and decreases the visual contrast between GM and WM in FA images. The regional variation of the precision of FA measurements agrees with recently reported results (34) that used multiple subjects and a statistical parametric mapping approach. One implication of the above result is that group analysis studies cannot achieve unbiased high SNR results by averaging data from multiple subjects if the DTI data acquired for each subject was of low SNR. Great care should therefore be taken to ensure sufficient SNR in the individual DTI datasets. Additionally, an equal number of DTI scans should be used for patients and controls to avoid a mismatch of SNR that could obscure group changes in FA values.

The precision of DTI-contrasts can be visualized as a function of the underlying PEV orientation. It can be seen in Fig. 2 that the 30-direction DW scheme used in this study provides a largely uniform precision profile. A further extension of this method is that it may provide a means to validate hardware calibration with in vivo DTI results and may elucidate subtle effects that are otherwise difficult to isolate in individual FA maps or in tractography results. In particular, poor precision or inaccuracy due to decreased magnetic field gradient stability, static field inhomogeneity, receive coil sensitivity, or DW contributions from background gradients may be discovered in this way.

The behavior of the sorted eigenvalues (λ_1, λ_2, and λ_3) as a function of SNR readily accounts for the observed FA and MD results and has been reported in simulation-based studies (23,24,26). In GM, the increase of λ_1 and concurrent decrease of λ_3 at low SNR accounts for the upward FA bias. However, as the biases in λ_1 and λ_3 largely offset each other, a stable MD value was observed over the range of SNR investigated in this study. The bias in the computed eigenvalues is due to the Rician noise properties of magnitude MR data and has been investigated by previous studies (24,27,42,43).

The investigation of the effect of SNR on the precision (reproducibility, both within and between scan sessions) of FA and MD found that though ROI-based measures of FA and MD are more reproducible than voxelwise measures, ROI-based analysis does not afford a solution to the problem of bias. This was illustrated for FA in Fig. 4. In ROI-based analysis, with 3 DTI scans, FA and MD measurements have an intrasession CV of less than 2% in the WM regions investigated, but an intrasession CV $\approx$ 5% in GM (Fig. 7a and b). In voxelwise analysis however (Fig. 6a and b), the precision of FA measurements in low FA regions is especially poor (intrasession CV $\approx$ 25%) with three DTI scans, though MD measurements are more robust (intrasession CV $\approx$ 5%).

Overall, an accurate and precise quantification of FA values in GM requires substantially more SNR (i.e., more DTI datasets) than the quantification of WM FA values. Our results indicate that an individual DTI scan of 30 DWI images + 5 b_0s at 1.5T provides satisfactory accuracy for the quantitative assessment of FA in WM regions. However, because the precision of voxel-wise FA measures is particularly sensitive to SNR, studies that investigate the diffusion anisotropy of WM structures near the cortical boundary together with cortical GM would be especially vulnerable to FA bias caused by low SNR and would likely require substantially more SNR than is typically acquired.

Previous studies (29,32) have shown that a DW scheme with a low number of unique directions can cause bias and unequal variability of DTI contrasts as a function of PEV orientation, and variability in the determination of the PEV orientation itself. In this study, which utilized a 30 orientation DW scheme, the precision of FA measurements showed no dependence on the orientation of the PEV. Further investigation of the effect of the DW scheme on in vivo human DTI studies is deferred to future work.

The precision of the PEV orientation was found to improve as a function of SNR, with an AV of approximately 6° to 3° in the range of one to three DTI scans. An approximately two-fold improvement in the precision of PEV measurements was observed when three DTI scans were used to calculate the diffusion tensor, relative to PEV maps that used only one DTI scan. The result that the PEV precision in the frontal WM is poor may be explained by the fact that this is a region of crossing fibers where each voxel contains two or more fiber populations. The observed PEV may therefore be especially sensitive to changes in the location of the imaged voxel relative to the underlying structure (interscan effects), together with partial volume and resolution effects, which could all contribute to poor PEV precision.

Notably, no significant AB was observed in the orientation of the PEV at low SNR relative to the gold stan-

dard PEV orientation. One consequence of upward FA bias and fidelity of the PEV orientation at low SNR is that the same FA termination criteria for tractography can produce very different results in the proximity of GM regions. It is conceivable that computed fibers from tractography may project into cortical or deep GM in a low SNR dataset, as the GM voxels exhibit elevated FA values and thus satisfy the FA tractography criteria, whereas the same GM voxel is excluded from tractography in a high SNR datasets because the voxel intensity has no upward FA bias.

In conclusion, the results from this study provide guidance for FA, MD, and PEV quantification and a means to investigate the minimal detectable differences within and across scan sessions as a function of SNR. In multicenter studies, where data compatibility is of primary importance, it is essential to confirm that a protocol is designed to achieve sufficient SNR to meet the aims of the study. Protocols designed in a low SNR regime could be highly sensitive to small differences in hardware performance, even if equivalent imaging parameters are adopted. To confront this, it is a recommendation of this study that imaging sites, particularly those in collaborative studies, should implement a protocol as a part of quality assurance testing to identify the appropriate SNR threshold necessary to achieve accurate (unbiased) DTI-derived contrasts, and should validate the compatibility of DTI data across different sites and scanners.

ACKNOWLEDGMENTS

Dr. Peter C.M. van Zijl is a paid lecturer for Philips Medical Systems. This arrangement has been approved by Johns Hopkins University in accordance with its conflict of interest policies. Dr. Craig K. Jones is supported by a grant to the Kennedy Krieger Institute by Philips Medical Systems

REFERENCES

1. Basser PJ, Mattiello J, LeBihan D. MR diffusion tensor spectroscopy and imaging. Biophys J 1994;66:259–267.
2. Beaulieu C. The basis of anisotropic water diffusion in the nervous system—a technical review. NMR Biomed 2002;15:435–455.
3. Beaulieu C, Allen PS. Determinants of anisotropic water diffusion in nerves. Magn Reson Med 1994;31:394–400.
4. Henkelman RM, Stanisz GJ, Kim JK, Bronskill MJ. Anisotropy of NMR properties of tissues. Magn Reson Med 1994;32:592–601.
5. Makris N, Worth AJ, Sorensen AG, et al. Morphometry of in vivo human white matter association pathways with diffusion-weighted magnetic resonance imaging. Ann Neurol 1997;42:951–962.
6. Moseley ME, Cohen Y, Kucharczyk J, et al. Diffusion-weighted MR imaging of anisotropic water diffusion in cat central nervous system. Radiology 1990;176:439–445.
7. Pierpaoli C, Jezzard P, Basser PJ, Barnett A, Di Chiro G. Diffusion tensor MR imaging of the human brain. Radiology 1996;201:637–648.
8. Horsfield MA, Jones DK. Applications of diffusion-weighted and diffusion tensor MRI to white matter diseases—a review. NMR Biomed 2002;15:570–577.
9. Ulug AM, Beauchamp N Jr, Bryan RN, van Zijl PC. Absolute quantitation of diffusion constants in human stroke. Stroke 1997;28:483–490.
10. van Gelderen P, de Vleeschouwer MH, DesPres D, Pekar J, van Zijl PC, Moonen CT. Water diffusion and acute stroke. Magn Reson Med 1994;31:154–163.
11. Mori S, van Zijl PC. Fiber tracking: principles and strategies—a technical review. NMR Biomed 2002;15:468–480.
12. Lim KO, Helpern JA. Neuropsychiatric applications of DTI—a review. NMR Biomed 2002;15:587–593.
13. Le Bihan D, van Zijl P. From the diffusion coefficient to the diffusion tensor. NMR Biomed 2002;15:431–434.
14. Basser PJ, Jones DK. Diffusion-tensor MRI: theory, experimental design and data analysis—a technical review. NMR Biomed 2002;15:456–467.
15. Pajevic S, Pierpaoli C. Color schemes to represent the orientation of anisotropic tissues from diffusion tensor data: application to white matter fiber tract mapping in the human brain. Magn Reson Med 1999;42:526–540.
16. Basser PJ, Pajevic S, Pierpaoli C, Duda J, Aldroubi A. In vivo fiber tractography using DT-MRI data. Magn Reson Med 2000;44:625–632.
17. Conturo TE, Lori NF, Cull TS, et al. Tracking neuronal fiber pathways in the living human brain. Proc Natl Acad Sci USA 1999;96:10422–10427.
18. Lazar M, Weinstein DM, Tsuruda JS, et al. White matter tractography using diffusion tensor deflection. Hum Brain Mapp 2003;18:306-321.
19. Mori S, Crain BJ, Chacko VP, van Zijl PC. Three-dimensional tracking of axonal projections in the brain by magnetic resonance imaging. Ann Neurol 1999;45:265–269.
20. Parker GJ, Stephan KE, Barker GJ, et al. Initial demonstration of in vivo tracing of axonal projections in the macaque brain and comparison with the human brain using diffusion tensor imaging and fast marching tractography. Neuroimage 2002;15:797–809.
21. Poupon C, Clark CA, Frouin V, et al. Regularization of diffusion-based direction maps for the tracking of brain white matter fascicles. Neuroimage 2000;12:184–195.
22. Xue R, van Zijl PC, Crain BJ, Solaiyappan M, Mori S. In vivo three-dimensional reconstruction of rat brain axonal projections by diffusion tensor imaging. Magn Reson Med 1999;42:1123–1127.
23. Pierpaoli C, Basser PJ. Toward a quantitative assessment of diffusion anisotropy. Magn Reson Med 1996;36:893–906.
24. Anderson AW. Theoretical analysis of the effects of noise on diffusion tensor imaging. Magn Reson Med 2001;46:1174–1188.
25. Armitage PA, Bastin ME. Utilizing the diffusion-to-noise ratio to optimize magnetic resonance diffusion tensor acquisition strategies for improving measurements of diffusion anisotropy. Magn Reson Med 2001;45:1056–1065.
26. Bastin ME, Armitage PA, Marshall I. A theoretical study of the effect of experimental noise on the measurement of anisotropy in diffusion imaging. Magn Reson Imaging 1998;16:773–785.
27. Jones DK, Basser PJ. "Squashing peanuts and smashing pumpkins": how noise distorts diffusion-weighted MR data. Magn Reson Med 2004;52:979–993.
28. Alexander DC, Barker GJ. Optimal imaging parameters for fiber-orientation estimation in diffusion MRI. Neuroimage 2005;27:357–367.
29. Jones DK. The effect of gradient sampling schemes on measures derived from diffusion tensor MRI: a Monte Carlo study. Magn Reson Med 2004;51:807–815.
30. Xing D, Papadakis NG, Huang CL, Lee VM, Carpenter TA, Hall LD. Optimised diffusion-weighting for measurement of apparent diffusion coefficient (ADC) in human brain. Magn Reson Imaging 1997;15:771–784.
31. Jones DK, Horsfield MA, Simmons A. Optimal strategies for measuring diffusion in anisotropic systems by magnetic resonance imaging. Magn Reson Med 1999;42:515–525.
32. Skare S, Hedehus M, Moseley ME, Li TQ. Condition number as a measure of noise performance of diffusion tensor data acquisition schemes with MRI. J Magn Reson 2000;147:340–352.
33. Jones DK. Determining and visualizing uncertainty in estimates of fiber orientation from diffusion tensor MRI. Magn Reson Med 2003;49:7–12.
34. Marenco S, Rawlings R, Rohde GK, et al. Regional distribution of measurement error in diffusion tensor imaging. Psychiatry Res 2006;147:69–78.
35. Pfefferbaum A, Adalsteinsson E, Sullivan EV. Replicability of diffusion tensor imaging measurements of fractional anisotropy and trace in brain. J Magn Reson Imaging 2003;18:427–433.

36. Landman BA, Farrell JA, Mori S, van Zijl PCM, Prince JL. On the coregistration of diffusion weighted images. In: Proceedings of the 14th Annual Meeting of the ISMRM, Seattle, WA, USA, 2006 (Abstract 2987).
37. Jenkinson M, Bannister P, Brady M, Smith S. Improved optimization for the robust and accurate linear registration and motion correction of brain images. Neuroimage 2002;17:825–841.
38. Basser PJ, Pierpaoli C. Microstructural and physiological features of tissues elucidated by quantitative-diffusion-tensor MRI. J Magn Reson B 1996;111:209–219.
39. Jiang H, Golay X, van Zijl PC, Mori S. Origin and minimization of residual motion-related artifacts in navigator-corrected segmented diffusion-weighted EPI of the human brain. Magn Reson Med 2002; 47:818–822.
40. Jones DK, Pierpaoli C. Contribution of cardiac pulsation to variability of tractography results. In: Proceedings of the 13th Annual Meeting of the ISMRM, Miami Beach, FL, USA, 2005 (Abstract 222).
41. Pierpaoli C, Marenco S, Rohde G, Jones DK, Barnett AS. Analyzing the contribution of cardiac pulsation to the variability of quantities derived from the diffusion tensor. In: Proceedings of the 11th Annual Meeting of the ISMRM, Toronto, Ontario, Canada, 2003 (Abstract 70).
42. Edelstein WA, Bottomley PA, Pfeifer LM. A signal-to-noise calibration procedure for NMR imaging systems. Med Phys 1984;11:180–185.
43. Gudbjartsson H, Patz S. The Rician distribution of noisy MRI data. Magn Reson Med 1995;34:910–914.